PROCEEDINGS OF SPIE

SPIEDigitalLibrary.org/conference-proceedings-of-spie

Passive LWIR hyperspectral imaging of surfaces contaminated by CWA droplets

L. Landström, F. Kullander, P. Wästerby, B. T. Røen

L. Landström, F. Kullander, P. Wästerby, B. T. Røen, "Passive LWIR hyperspectral imaging of surfaces contaminated by CWA droplets," Proc. SPIE 11010, Chemical, Biological, Radiological, Nuclear, and Explosives (CBRNE) Sensing XX, 1101013 (17 May 2019); doi: 10.1117/12.2520420

SPIE.

Event: SPIE Defense + Commercial Sensing, 2019, Baltimore, Maryland, United States

Downloaded From: https://www.spiedigitallibrary.org/conference-proceedings-of-spie on 16 Oct 2019 Terms of Use: https://www.spiedigitallibrary.org/terms-of-use

Passive LWIR hyperspectral imaging of surfaces contaminated by CWA droplets

L. Landström[a][1], F. Kullander[b], P. Wästerby[a], B. T. Røen[c]

[a]Swedish Defence Research Agency (FOI), CBRN Defence and Security, Cementvägen 20, SE-901 82, Umeå, Sweden
[b]Swedish Defence Research Agency (FOI), C4ISR, Olaus Magnus väg 42, SE-583 30, Linköping, Sweden
[c]Norwegian Defence Research Establishment (FFI), P.O. Box 25, NO-2027, Kjeller, Norway

ABSTRACT

A passive LWIR camera based on a focal plane array detector was used to capture hyperspectral images of different scenes where low volatile chemical warfare agent (CWA) and simulant droplets were deposited on a variety of substrates. Four different CWA; mustard gas (HD), cyclosarin (GF), VX, VR, and two simulant liquids; dimethyl methylphosphonate (DMMP) and triethyl phosphate (TEP) were used as surface contaminants and applied to the substrates as 5 µl droplets. The trials were performed outdoors with the scene close to the ground and the camera imaging at an angle of approximately 35° and a stand-off distance of about 2 m, i.e., mainly the reflected radiation from the cold sky in combination with the thermal emission from the scene were observed. Brightness temperature spectra were extracted from the hyperspectral data cubes and compared to results from a thin film model as well as reference LWIR spectra of the liquids.

Keywords: LWIR, infrared, imaging, hyperspectral, chemical warfare agent, detection, surface contamination, nerve agent

1. INTRODUCTION

There is a demand for improved technologies/capabilities to scan different areas with the purpose of detecting and locating surface contaminants. If the contamination consists of a highly toxic material, such as persistent chemical warfare agents (CWA), an instrument that provides high confidence, efficient examination of large surfaces also preferably at a remote location from the contamination is obviously highly desired. Current spectroscopic devices commonly operate as point detectors, e.g., handheld Raman systems, which then becomes slow and labor intensive if being applied for surface detection purposes. Hyperspectral imaging techniques would enable far more efficient scanning over larger areas compared to point detectors, with the possibility to also achieve a high spatial (pixel) resolution. Different spectroscopic techniques have been identified as promising for hyperspectral imaging purposes, such as active methods based on Raman spectroscopy or IR illumination. [1-10]

An established technology, already fielded for purposes like chemical cloud detection and monitoring, is the passive hyperspectral LWIR imaging technique. In such imaging instruments (both array and scanning single detector devices) the hyperspectral information is usually retained by using an interferometer, where the measured interferogram from the instantaneous field of view of each spatial element (pixel) is transformed to the frequency domain to yield spectral information. Characteristic spectral signatures from chemicals present in the field of view of the instrument can appear both as a result of molecular thermal emission and absorption of background radiation. When a passive IR system is instead used to image different surfaces and liquid/solid contaminants thereon, other optical phenomena such as interference may further influence the measured radiance (or related brightness temperature), e.g., if the droplet is optically thin. Droplet geometry, such as high curvature, may also additionally complicate the situation compared to an ideal, thin film scenario.

In the present report, results from passive measurements of different scenes using a commercial LWIR hyperspectral camera are presented. Measurements were performed outdoors on substrates such as military paint systems, tiles, and aluminum mirrors together with brushed aluminum plates, with the latter being treated as Lambertian surfaces to monitor the radiative influx. A comparison of measured data to a thin film model [11] is also presented, and good conformity could be seen, especially when including measured data from the Lambertian surface (i.e., incoming radiation from the sky).

[1] lars.landstrom@foi.se; phone +46 90 106750; www.foi.se

Chemical, Biological, Radiological, Nuclear, and Explosives (CBRNE) Sensing XX
edited by Jason A. Guicheteau, Chris R. Howle, Proc. of SPIE Vol. 11010, 1101013
© 2019 SPIE · CCC code: 0277-786X/19/$18 · doi: 10.1117/12.2520420

Downloaded From: https://www.spiedigitallibrary.org/conference-proceedings-of-spie on 16 Oct 2019
Terms of Use: https://www.spiedigitallibrary.org/terms-of-use

Finally, the different spectral response of live agents and simulants on a number of substrates are shown and briefly discussed.

2. EXPERIMENTAL

A commercial LWIR camera was used to acquire the hyperspectral images (HSI) of the different scenes, with a measurement setup as illustrated in Figure 1. The system was set to a 4 cm^{-1} spectral resolution, 330 µs integration time and 256 × 256 elements of the focal plane array detector were being used. The set up was radiologically calibrated before the measurement series.

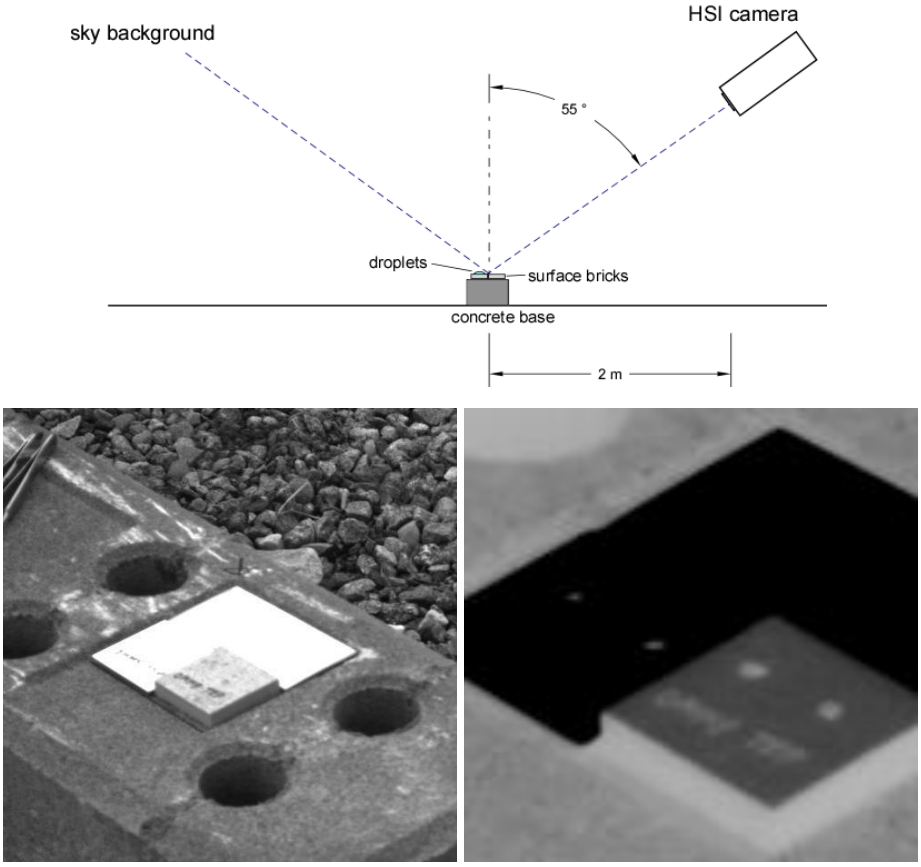

Figure 1. Top) Measurement geometry during the outdoor trial. Lower left panel) Visible, grayscale image of a typical arrangement of the scene; two quadratic plates (50 mm × 50 mm) with 5 µl droplets beside a rectangular, brushed Al plate (approximately Lambertian). Lower right panel) Broadband thermal image of the scene captured by the HSI instrument.

Different 50 mm × 50 mm substrates were investigated; Al mirror, gray and green paint systems and two different tiles. The agents and simulants being used are listed in Table 1, and these were deposited as 5 µl liquid droplets onto the substrates which were then placed onto a concrete block (see Figure 1). An example of a broadband thermal image of one of the scenes is also depicted in Figure 1.

Downloaded From: https://www.spiedigitallibrary.org/conference-proceedings-of-spie on 16 Oct 2019
Terms of Use: https://www.spiedigitallibrary.org/terms-of-use

Table 1. Simulant chemicals and CWA used in the experiments.

Abbr.	Name	Provider	Notes	CAS#
DMMP	Dimethyl methylphosphonate	Merck	>97%	756-79-6
TEP	Triethyl phosphate	Merck	>99 %	78-40-0
VX	VX	In house	>98% NMR	50782-69-9
VR	Russian VX	In house	>98% NMR	159939-87-4
GF	Cyclosarin	In house	>98% NMR	329-99-7
HD	Sulfur mustard/Mustard gas	In house	>99% GC-MS	505-60-2

The brightness of the sky background was varying during the course of the trial as a result of partly cloudy conditions. A measure of the current spectral radiance was obtained by placing strong diffusely scattering surfaces (brushed Al plates) in the field of view of the camera beside the substrates (see Figure 1). The air temperature and relative humidity (RH) as reported from a local weather station were around 8 °C and RH 65%. Cloud data were not available from the weather station but images from the trial gave the impression of relatively high and thin clouds. Simulations of the incoming radiance for different cloud conditions and for the geometry in the trial were carried out using the program package *MODTRAN* [12]. The results, as shown in Figure 2, are qualitatively in good agreement with the spectral radiance observed from the high reflectance surfaces. Emission due to ozone (~1000-1100 cm^{-1}) and water emission lines, present in the model results, could also be observed in the experimental data.

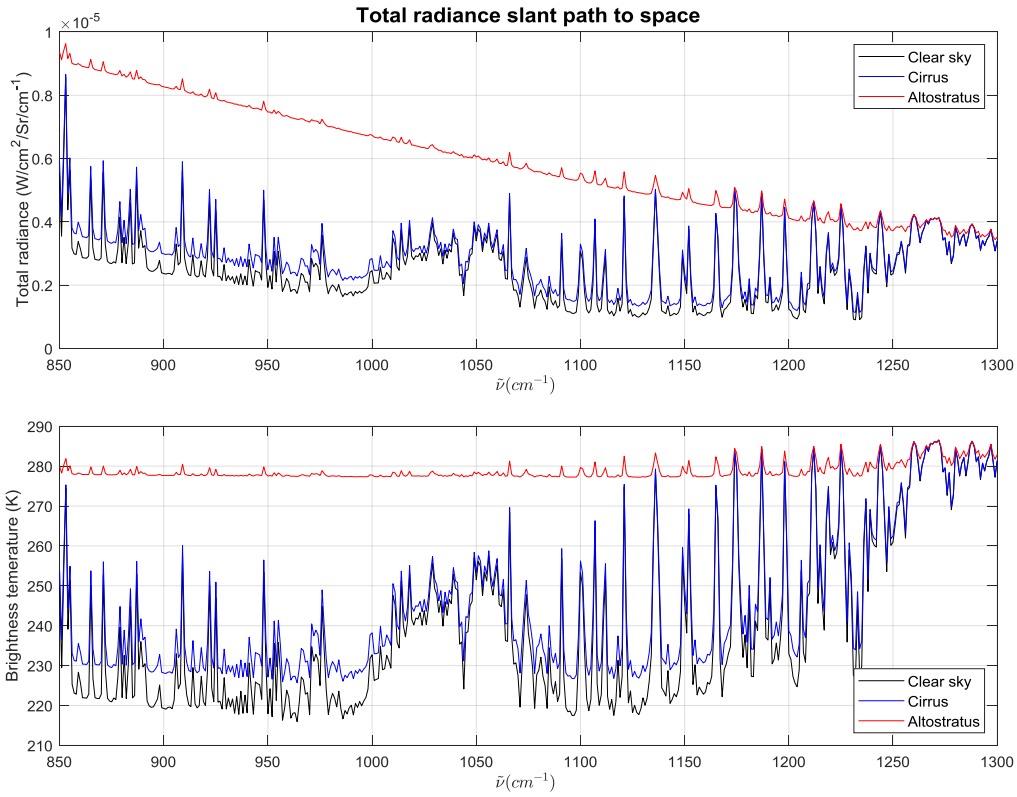

Figure 2. Top) Simulated spectral radiance (1 cm^{-1} resolution) emitted by the atmosphere (including thermal radiation reflected by the ground and scattered by the atmosphere) using the model 'SubArctic Summer' for the three cases; clear sky (black), cirrus clouds (blue) and altostratus clouds at 2.4 km cloud base (red). Bottom) Corresponding brightness temperatures.

Downloaded From: https://www.spiedigitallibrary.org/conference-proceedings-of-spie on 16 Oct 2019
Terms of Use: https://www.spiedigitallibrary.org/terms-of-use

3. MODEL

We adopt the thin film layer model used in refs. [7, 11] to calculate the received spectral radiance; $L = L_e + L_r$, where L_e denotes the emitted and L_r the reflected radiance, under the assumption that the attenuation in the air between the surface and the camera is negligible. The interfaces are assumed smooth and flat so that coherent addition of reflected optical fields occurs. We have also compared this approach to an incoherent optical analysis, see for example ref. [13] related to the work in ref. [1] and the modelling results from the two approaches are very similar as long as the radiative contribution from the second interface (liquid/solid substrate) is negligible. Interference fringes as a function of wavenumber develop in this thin film layer model under conditions where the radiation from the second interface becomes significant, i.e., when there is a sufficiently high transmission through the contamination layer (optically thin). A more accurate treatment, e.g., incorporating the phase structure function of the optical field and also the surface roughness of the solid interface, can be expected to reduce these interference fringes.

The contaminated surface is approximated by a thin liquid slab with planar interfaces to the air and to the solid substrate surface, see Figure 3. Furthermore, the liquid and the solid material are modelled as homogeneous absorbing dielectric materials in thermal equilibrium. Only specular reflection is treated and scattering is not taken into account. Required input parameters to the model include the complex index of refraction, here denoted as $\tilde{n}_i = n_i + i\kappa_i$, for each of the domains, the surface temperature T and the incident spectral radiance L_{in}.

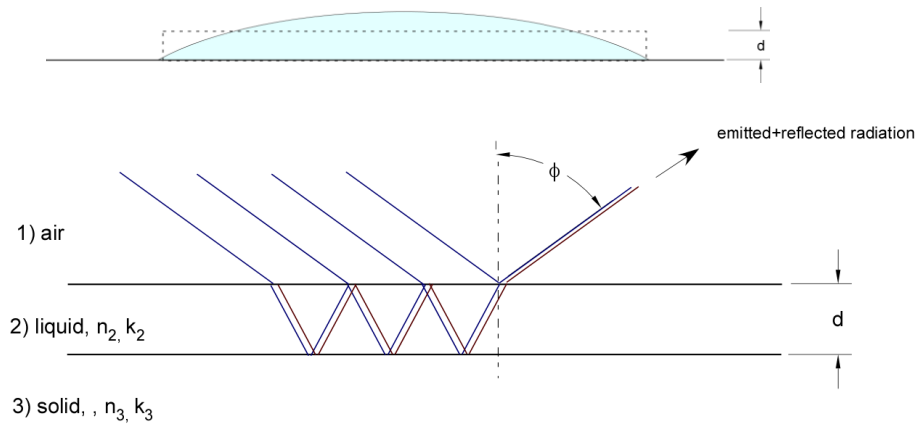

Figure 3. Reflection/emission from a liquid film layer on a solid surface. Droplet (contamination) is modeled as a cylinder with the height, *d*, depending on volume and radius.

Let R denote the reflectance of the contaminated surface and $L_{bb}(T)$ the blackbody spectral radiance, then the reflected and emitted spectral radiance will be given by $L_r = RL_{in}$ and $L_e = (1 - R)L_{bb}(T)$, resulting in the received, frequency dependent, spectral radiance:

$$L = RL_{in} + (1 - R)L_{bb}(T). \tag{1}$$

The reflectance for *s*- and *p*-polarization as a function of the (field) reflection coefficients ($r_{ij,s}$, $r_{ij,p}$) and the complex phase shift, δ, imposed by transmission through the liquid slab can be shown to be [11]:

$$R_s = \left|\frac{r_{12,s}+r_{23,s}e^{-2i\delta}}{1+r_{12,s}r_{23,s}e^{-2i\delta}}\right|^2 \text{ and } R_p = \left|\frac{r_{12,p}+r_{23,p}e^{-2i\delta}}{1+r_{12,p}r_{23,p}e^{-2i\delta}}\right|^2, \tag{2}$$

with δ given by:

$$\delta = 2\pi\tilde{\nu}d\sqrt{\tilde{n}_2 - sin^2\theta_1}. \tag{3}$$

Downloaded From: https://www.spiedigitallibrary.org/conference-proceedings-of-spie on 16 Oct 2019
Terms of Use: https://www.spiedigitallibrary.org/terms-of-use

Here, $\tilde{\nu}$ denotes the wavenumber $(1/\lambda)$. For unpolarized incoming radiation the contaminated surface reflectance then becomes:

$$R = \frac{R_s + R_p}{2}. \tag{4}$$

Furthermore, Fresnel's equations are used to compute the reflection coefficients for the interfaces as a function of incidence angle and the frequency dependent optical properties of the material:

$$r_{ij,s} = \frac{\tilde{n}_i \cos\theta_i - \tilde{n}_j \sqrt{1-\left(\tilde{n}_i \tilde{n}_j^{-1} \sin\theta_i\right)^2}}{\tilde{n}_i \cos\theta_i + \tilde{n}_j \sqrt{1-\left(\tilde{n}_i \tilde{n}_j^{-1} \sin\theta_i\right)^2}} \text{ and } r_{ij,p} = \frac{\tilde{n}_i \sqrt{1-\left(\tilde{n}_i \tilde{n}_j^{-1} \sin\theta_i\right)^2} - \tilde{n}_j \cos\theta_i}{\tilde{n}_i \sqrt{1-\left(\tilde{n}_i \tilde{n}_j^{-1} \sin\theta_i\right)^2} + \tilde{n}_j \cos\theta_i}. \tag{5}$$

Finally, the reflectance of each component at each interface is then given by the squared modulus, $R_{ij} = \left|r_{ij}\right|^2$.

We modelled the received spectral radiance for two of the simulant contaminants used in the trial, DMMP and TEP, where n, κ-values for these compounds were taken from [14]. Figure 4 depicts the n, κ-values in the spectral band of interest as well as calculated reflectances for the air/liquid interface.

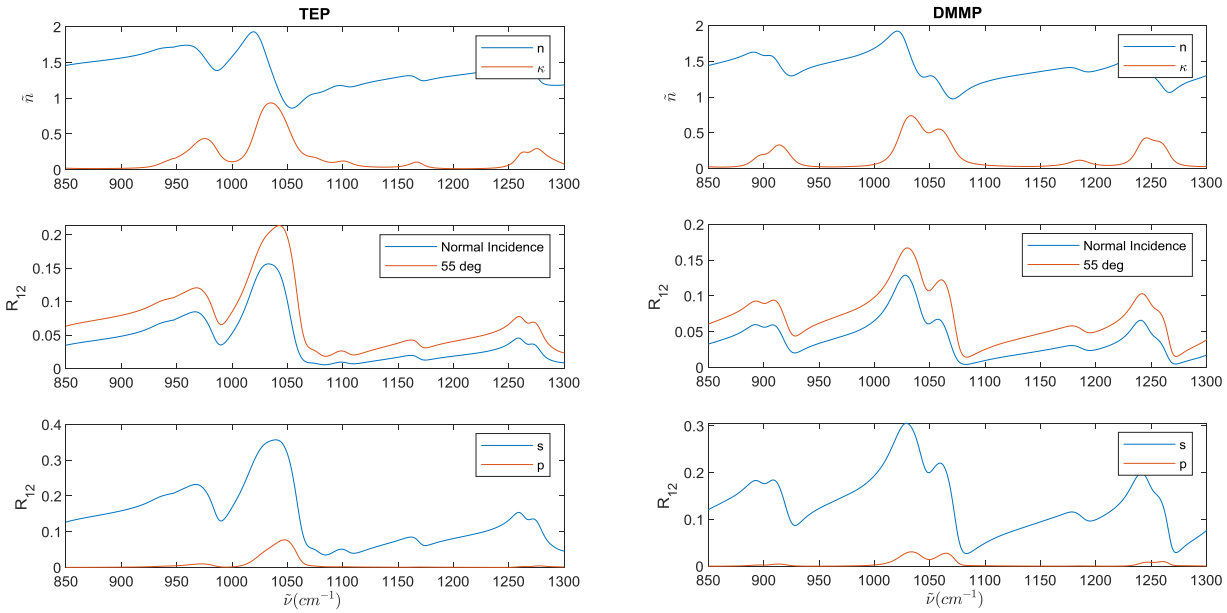

Figure 4. Complex index of refraction and calculated reflectance for the air/liquid interface in the spectral region of interest for TEP and DMMP.

We currently do not have complex index of refraction data for all the investigated substrate surfaces and either use data for aluminum to represent a high reflectance surface, or simulated values to represent a low reflectance surface in the model. Liquid layer depths in the range of 10-200 µm were modelled and compared to experimental data (as this is the approximated range of depth of the droplets in the trial based on applied volume and droplet diameters). The surface temperature used in the model was adapted to conform to the measured brightness temperature level in the acquired data. As a final input to the model, the measured spectral radiance from the roughened Al plate was used as the incident spectral radiance. The modelled spectral radiance was then converted to brightness temperature by inversion of Planck's law.

Downloaded From: https://www.spiedigitallibrary.org/conference-proceedings-of-spie on 16 Oct 2019
Terms of Use: https://www.spiedigitallibrary.org/terms-of-use

4. RESULTS & DISCUSSION

Spectra averaged from subgroups of pixels within the liquid contamination, the clean substrate background, and the reference surface were extracted from the HSI data cube and examined. The number of pixels used for the liquid contamination was adapted to its distribution and varied between 1 and 100. Data from only a few pixels (1-3) had to be used for small droplets with high curvature.

Extracted brightness temperature spectra for TEP on brown tile and the Al mirror surface are shown in Figure 5 as a typical example. The spectra from the contamination generally appear around a level that can be judged to be close to the temperature of the surface. However, on the mirror surfaces a slightly lower average brightness temperature could be observed. As all contaminants exhibited poor wetting on this substrate, resulting in small droplets with a high curvature, we attribute this effect mainly to droplet geometry.

Features that can be associated with both the contaminant and the sky background can typically be discerned in the spectra. Spectral features associated with the clean background surfaces are generally having a relatively low contrast compared to those from the contaminated surface, and these features are typically not seen in the spectra from the contaminated surface.

The aluminum mirror surface reflects the incident sky radiation in close coincidence with that of the Lambertian surface, in particular for the example shown in Figure 5. The reflected radiance from the Lambertian surfaces varied as a function of the sky conditions during the trial, yielding brightness temperature spectra ranging between 220 and 280 K (see also Figure 2).

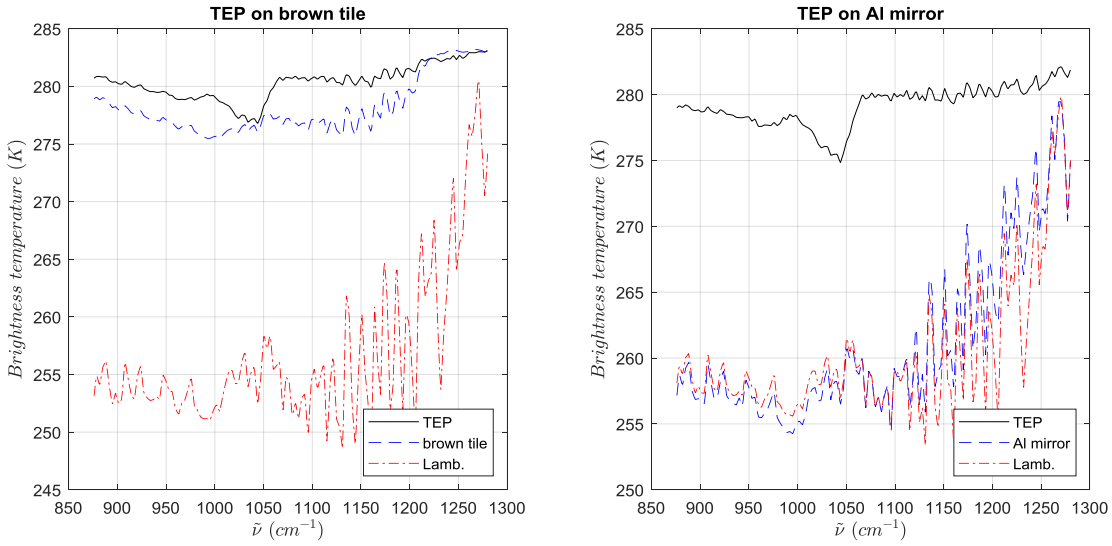

Figure 5. Brightness temperature spectra from contamination compared to that from background surface (brown tile or aluminum mirror) and from the roughened reference surface (approximately Lambertian).

Figure 6 compares spectra from a single HSI frame with averages from several frames taken at a frame rate of 1 Hz. The averaging does not improve the spectrum much for this level of contrast which is in accordance with the low noise equivalent spectral radiance (NESR = 20 nW/cm^2/sr/cm^{-1}) specified for the instrument. The right hand plot shows all single spectra from the 253 frames captured during one acquisition series. The level is changing but the shape stays the same which can be expected because of a small drift in surface temperature and change in droplet geometry during the measurement series. It can be seen that this varying level results in a slight smoothing of the spectrum averaged from 100 frames. However, we have selected to present the rest of the data with a 10 frame averaging.

Downloaded From: https://www.spiedigitallibrary.org/conference-proceedings-of-spie on 16 Oct 2019
Terms of Use: https://www.spiedigitallibrary.org/terms-of-use

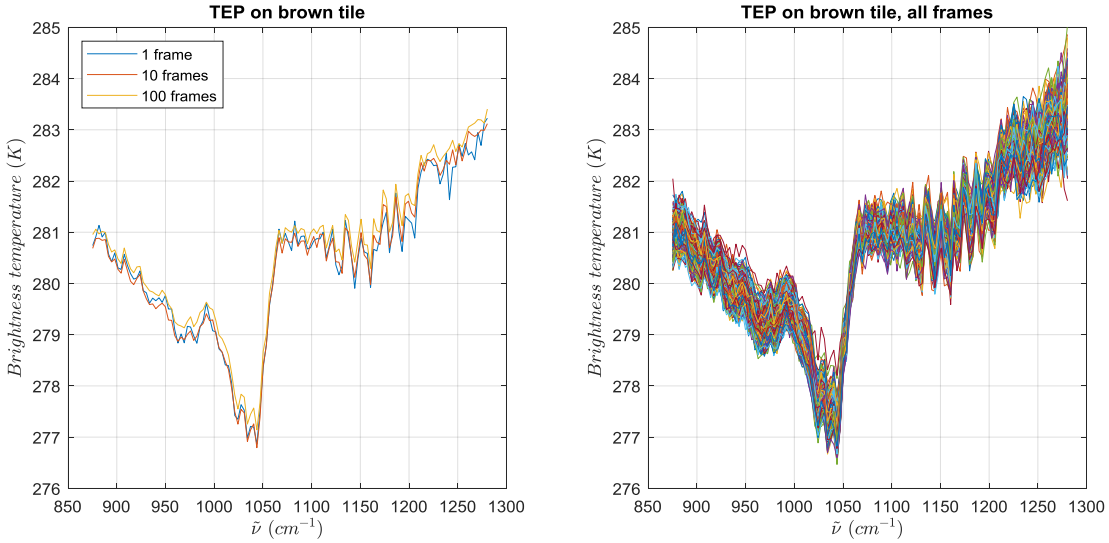

Figure 6. Series of spectra with TEP on brown tile. Left) Spectrum retrieved from 1 frame compared to averages of 10 and 100 frames. Right) All 253 frames during one recording.

Figure 7 and Figure 8 display spectra for TEP and DMMP on brown tile and on the mirror surface in comparison to simulated spectra. The measured incident radiance from the Lambertian surface was used as an input in the model. As previously stated, the surface temperature in the model was adjusted to yield a brightness temperature level matched to the measured spectra. We are aware that the modelled temperature can be slightly different from the actual physical surface temperature but the small adjustment will mainly result in a linear scaling of the spectral (brightness temperature) level.

The graphs display modeled spectra for three liquid layer depths and a good match to the measured spectra is obtained for all except the thinnest modeled layer on the highly reflective surface. This indicates that the liquid layers during the trials were thicker than 10 µm which is also what would be expected based on the measured areas covered by the 5 µl droplets.

As can be seen, for the low reflectance surface case (Figure 7), a layer thickness in the selected range will not have any substantial impact on the result. This is because the background surface reflection gives a negligible contribution leading to a reflectance mainly determined by the air/liquid interface (R_{12}). That is, mainly the emission from the liquid and reflection from the sky will contribute to the measured spectral radiance. The modelling also shows that the background surface will contribute in the high reflectance substrate case with a contamination layer thickness around 10 µm or below. Thus, the characteristics of the spectrum would be expected to change substantially for such thin layers on high reflective surfaces.

Downloaded From: https://www.spiedigitallibrary.org/conference-proceedings-of-spie on 16 Oct 2019
Terms of Use: https://www.spiedigitallibrary.org/terms-of-use

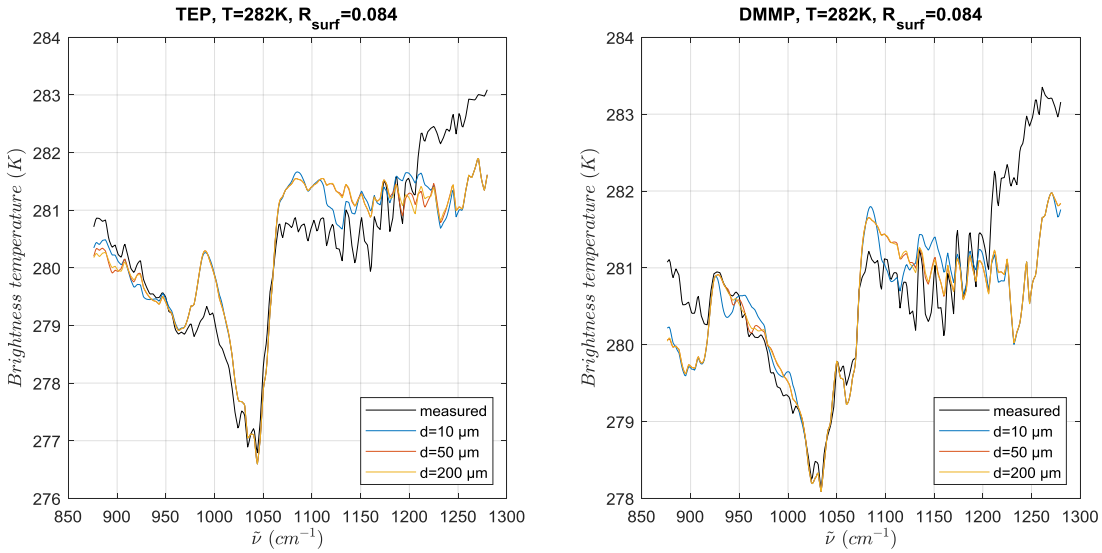

Figure 7. Measured spectra from TEP and DMMP on the brown tile compared to modelled spectra with settings according to titles and legends.

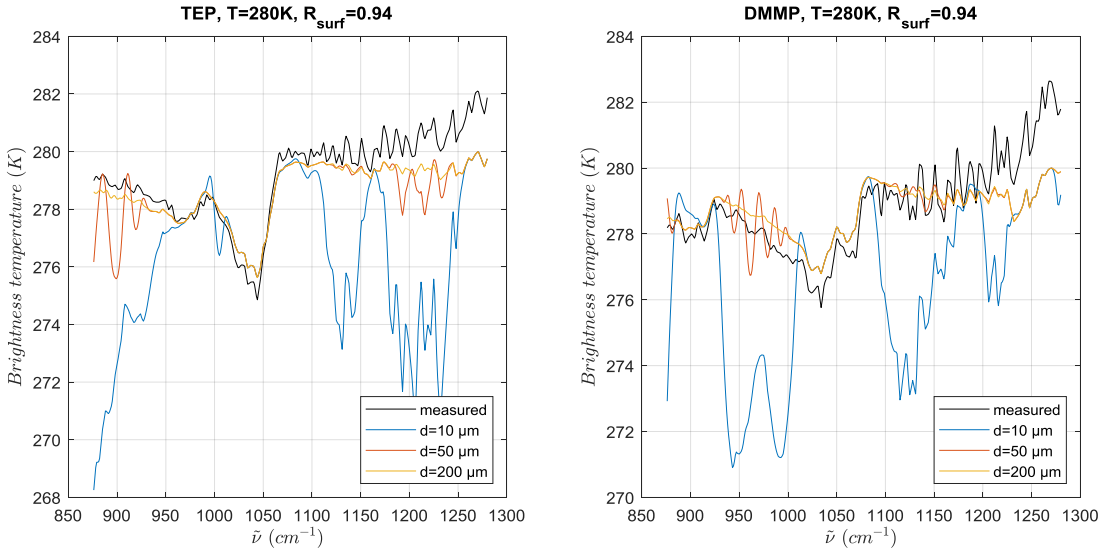

Figure 8. Measured spectra from TEP and DMMP on the Al mirror surface compared to modelled spectra with settings according to titles and legends.

The experimental data deviate from the model at high frequencies where it appears that the radiance from the sky background is not accurately modeled. Clearly, one possibility is that the spectral radiance from the Lambertian surface is not representative for the actual sky radiance in the line of sight. Another possible explanation is that the combined emitted and reflected radiance to the field of view of the instrument is affected by the curved shape of the liquid surface. In general, the radii of the applied droplets was smaller on the mirror and white tile surfaces compared to the other surfaces, thus implying more curvature.

The series of spectra obtained on different background surfaces for the above two described and modelled simulant chemicals as well as the CWA are displayed in Figure 9 to Figure 11. Due to the lack of complex index of refraction data for the CWA, a comparison is made to measured ATR (attenuated total reflection) transmission spectra. An accurate match

Downloaded From: https://www.spiedigitallibrary.org/conference-proceedings-of-spie on 16 Oct 2019
Terms of Use: https://www.spiedigitallibrary.org/terms-of-use

with the model is therefore not expected but spectral features connected to the absorption properties of the substances can be recognized.

The series of brightness temperature spectra for the contaminated surfaces are generally characterized by a mixture of a pattern similar to the sky radiance spectrum and spectral features related to the optical properties of the contaminant. Spectral features seen in pristine substrate surfaces are generally not present in the contaminated surface spectra.

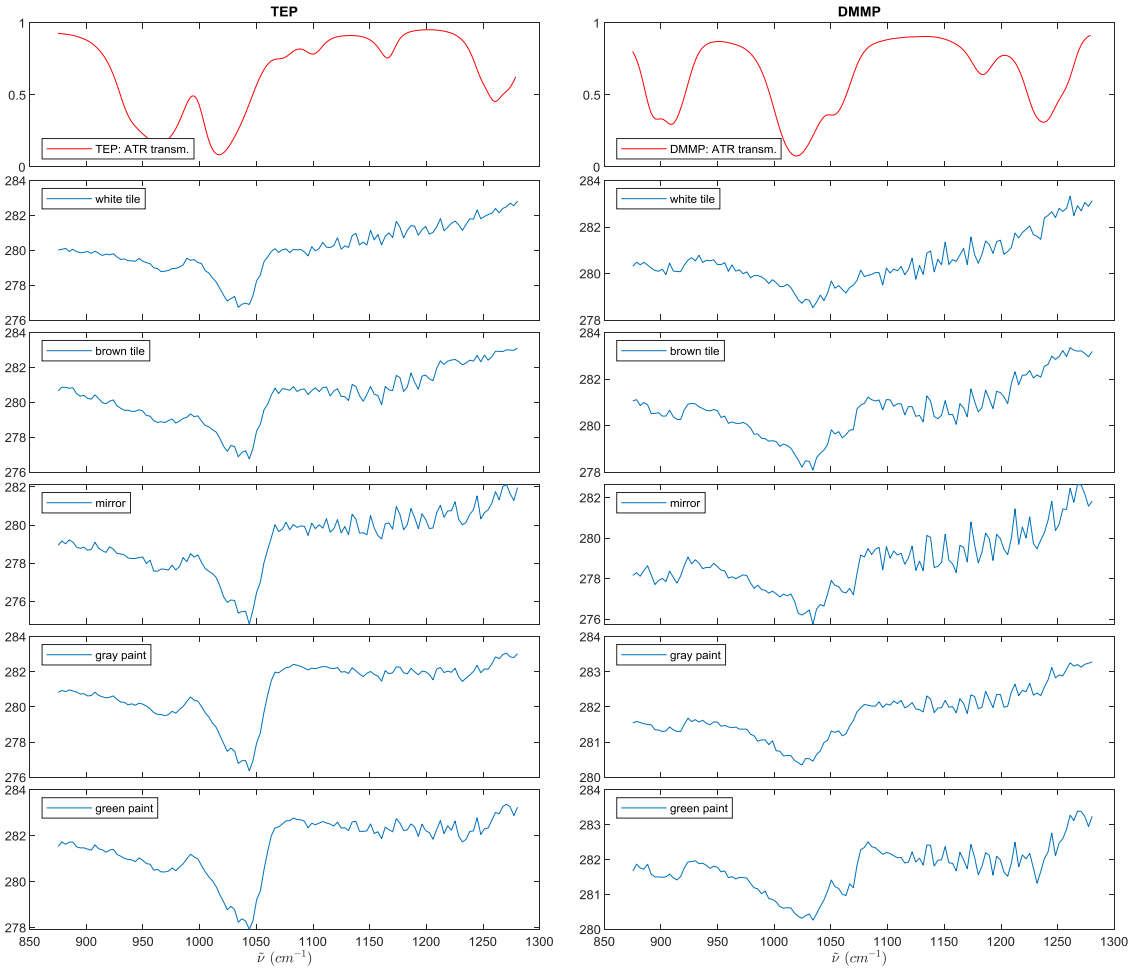

Figure 9. Brightness temperature for TEP and DMMP droplets on different test surfaces compared to measured ATR transmission. (Top panel y-axis is "Transmission" and for the lower panels "Brightness Temperature (K)".)

Figure 9 shows spectra from TEP and DMMP droplets on all substrates investigated. Both of these chemicals have relatively strong absorption features in this spectral range as can be seen in the ATR transmission spectrum. It can therefore be assumed that their corresponding reflectance features have relatively high contrast. The spectra obtained from TEP are in relatively good agreement with this assumption and the main spectral feature around 1040 cm^{-1} is easily discerned for all substrates with a brightness temperature contrast in the order of 3-4 K.

Downloaded From: https://www.spiedigitallibrary.org/conference-proceedings-of-spie on 16 Oct 2019
Terms of Use: https://www.spiedigitallibrary.org/terms-of-use

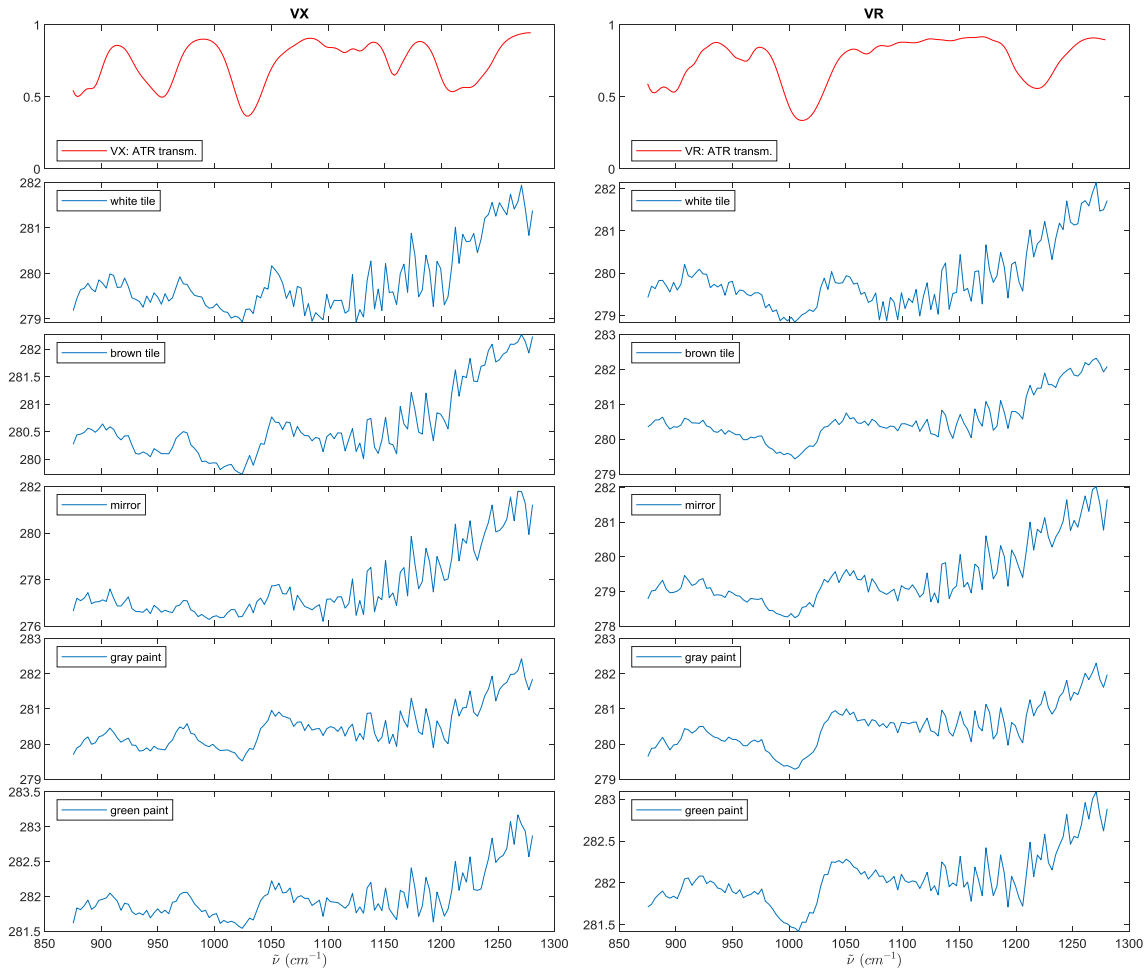

Figure 10. Brightness temperature for V-agent droplets on different test substrates compared to measured ATR transmission. (Top panel y-axis is "Transmission" and for the lower panels "Brightness Temperature (K)".)

For DMMP, the spectra from the brown tile and the painted surfaces further supports the above assumption with a contrast around 1.5-3 K for the main spectral feature. The lower contrast seen both on the white tile and on the mirror is currently not thoroughly understood. The reflected sky radiance from the reference surface was similar during all the acquisitions with DMMP. The lower contrast obtained on the mirror surface is possibly explained by droplet surface curvature as discussed above, leading to a larger fraction of reflected relative emitted radiation into the observed field of view. The unexpectedly low brightness temperature from the contamination on the mirror also supports this explanation.

The spectra for the V-agents, GF and HD applied on the different test substrates are shown in Figure 10 and 11. Spectral characteristics that can be associated to the ATR reference spectra in the 900-1050 cm^{-1} band are seen for both V-agents on all substrates. The brightness temperature contrast is in the order of 0.5-1 K except for the agents on white tile for which the contrast is smaller.

GF exhibits a brightness temperature contrast in the range of 1 K on all substrates with similarities seen compared to the absorption features shown in the ATR transmission spectrum. For HD, not much contrast can be expected in this range of wavenumbers, see top panel ATR measurement. Furthermore, as the temperature during the trials was around 8 °C, the HD droplets solidified on the substrates which likely increased the scattering from these deposits.

Downloaded From: https://www.spiedigitallibrary.org/conference-proceedings-of-spie on 16 Oct 2019
Terms of Use: https://www.spiedigitallibrary.org/terms-of-use

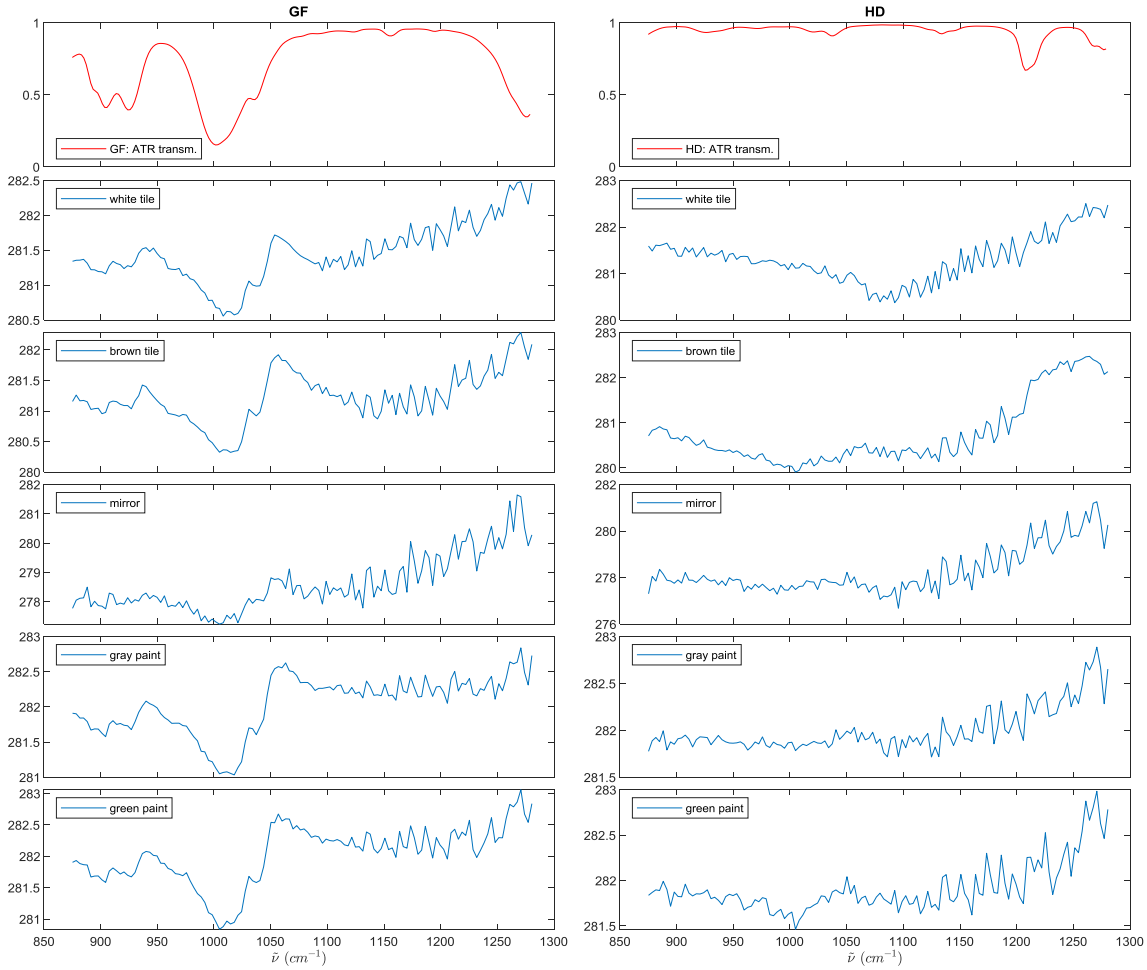

Figure 11. Brightness temperature for GF and HD droplets on different test substrates compared to measured ATR transmission. (Top panel y-axis is "Transmission" and for the lower panels "Brightness Temperature (K)".)

5. CONCLUSIONS

Measurements of contaminants on substrates with a passive, hyperspectral imaging (HSI) LWIR system indicate that the majority of the different contaminants (at the amounts and experimental conditions during the trial) can be detected and likely also classified. Modelling of the expected radiance by a coherent, thin film model showed good agreement with measured spectra. Importantly, for the droplet volumes and geometry used here, the observed brightness temperature spectra were almost independent on the substrate. Furthermore, the level of contrast is also dependent on the incoming (sky) radiance, e.g., a better contrast can be expected during night and/or clear skies. In addition, monitoring of the incoming sky radiance allows for separation of its contribution from measured spectra and/or for use as an input when modelling the expected radiance.

ACKNOWLEDGEMENTS

This work was funded by the Swedish Department of Defence, Project no. 410-A404119. The authors would also like to acknowledge Dr. Ove Gustavsson for the *MODTRAN* simulations.

Downloaded From: https://www.spiedigitallibrary.org/conference-proceedings-of-spie on 16 Oct 2019
Terms of Use: https://www.spiedigitallibrary.org/terms-of-use

REFERENCES

[1] Thériault, J.-M., Puckrin, E., Hancock, J., Lecavalier, P., Jackson Lepage, C. and Jensen, J. O., "Passive standoff detection of chemical warfare agents on surfaces", Appl. Opt., 43, 5870-5885 (2004).

[2] Farley, V., Vallières, A., Villemaire, A., Chamberland, M., Lagueux, P. and Giroux, J., "Chemical Agent Detection and Identification with a Hyperspectral Imaging Infrared Sensor", Proc. of SPIE Vol. 6739, 673918, (2007).

[3] Kalasinsky, K. S., Hadfield, T., Shea, A. A., Kalasinsky, V. F., Nelson, M. P., Neiss, J., Drauch, A. J., Vanni, G. S. and P. J. Treado, "Raman Chemical Imaging Spectroscopy Reagentless Detection and Identification of Pathogens: Signature Development and Evaluation", Anal. Chem., 79, 2658-2673 (2007).

[4] Howle, C. R., Stothard, D. J. M., Rae, C. F., Ross, M., Truscott, B. S., Dyer, C. D. and Dunn, M. H., "Active hyperspectral imaging system for the detection of liquids", Proc. SPIE, 6954, 69540L (2008).

[5] Blake, T. A., Kelly, J. F., Gallagher, N. B., Gassman, P. L. and Johnson, T. J., "Passive standoff detection of RDX residues on metal surfaces via infrared hyperspectral imaging", Anal. Bioanal. Chem., 395, 337-348 (2009).

[6] Siripatrawana, U., Makinob, Y., Kawagoeb, Y. and Oshita, S., "Rapid detection of Escherichia coli contamination in packaged fresh spinach using hyperspectral imaging", Talanta, 85, 276-281 (2011).

[7] Warren, R. E., Cohn, D. B., Gagnon, M.-A. and V. Farley. "Detecting liquid contamination on surfaces using hyperspectral imaging data", Proc. SPIE 9455, 94550M (2015).

[8] Thompson, J. V., Bixler, J. N., Hokr, B. H., Noojin, G. D., Scully M. O. and Yakovlev, V. V., "Single-shot chemical detection and identification with compressed hyperspectral Raman imaging", Opt. Lett., 42, 2169-2172, (2017).

[9] Landström, L., Kullander, F., Lundén, H. and Wästerby, P., "UV Raman imaging of surface contaminants using tunable laser and narrow bandpass filters", Proc. SPIE 10629, 1062907 (2018).

[10] Nordberg, M. and Landström, L., "UV Raman chemical imaging using compressed sensing", Analyst, 144, 1513-1518 (2019).

[11] Harig, R., Braun, R., Dyer, V et al., "Short-range remote detection of liquid surface contamination by active imaging Fourier transform spectrometry," Optics Express 16(8), 5708-5714 (2008).

[12] www.modtran.spectral.com (22 March 2019).

[13] Eismann, M. T., [Hyperspectral remote sensing] ISBN 978-0-8194-8787-2, SPIE Bellingham, (2012).

[14] Myers, T. L., Tonkyn, R. G., Oeck, A. M., Danby, T. O., Loring, J. S., Taubman, M. S., Sharpe, S. W., Birnbaum, J. C. and Johnson, T. J., "IARPA/PNNL Liquid Phase IR Spectra", https://webbook.nist.gov/chemistry/silmarils-liquids-n-k/ (22 March 2019).

Downloaded From: https://www.spiedigitallibrary.org/conference-proceedings-of-spie on 16 Oct 2019
Terms of Use: https://www.spiedigitallibrary.org/terms-of-use